Ionics
https://doi.org/10.1007/s11581-026-07454-7

RESEARCH

Controllable synthesis of multi-interfacial Cr-VO_2/Ni_3S_2 catalysts for efficient oxygen evolution reaction in alkaline freshwater and seawater

Haonan Wang[1] · Huipeng Zhao[1] · Xiaoshuang Zhang[2] · Xiaoqiang Du[1]

Received: 25 June 2026 / Revised: 31 July 2026 / Accepted: 10 August 2026

Abstract
Electrocatalytic overall water splitting (OWS) serves as a pivotal technical route for the scaled-up synthesis of green hydrogen. In this work, a Cr-VO_2/Ni_3S_2 multi-interfacial heterostructured catalyst was fabricated via a one-step hydrothermal strategy. Electrochemical measurements demonstrate that the catalyst delivers an overpotential of only 163 mV at 10 mA cm^{-2} in 1 M KOH electrolyte. In addition, it merely requires an overpotential of 165 mV to reach 10 mA cm^{-2} in 1 M KOH alkaline seawater electrolyte. Density functional theory further demonstrate that the Cr-VO_2 component can optimize the interfacial electronic configuration, accelerate charge transfer kinetics, and strengthen the water adsorption affinity of the catalyst. This work not only offers an innovative route for the structural fabrication and performance regulation of Ni_3S_2-based transition metal sulfides, but also delivers theoretical support and material support for the exploitation of low-cost and durable anodic catalysts applicable to both freshwater and seawater electrolysis.

Keywords Water splitting · Oxygen evolution reaction · Cr-VO_2/Ni_3S_2 · Multi-interfacial heterostructured catalyst · Density functional theory

Introduction

As the global energy structure accelerates its transition toward cleaner and low-carbon forms, developing sustainable, efficient, and environmentally friendly new energy carriers has become a critical breakthrough in addressing the energy crisis and environmental pollution [1–7]. Hydrogen, with its prominent advantages including outstanding energy storage density, environmental benignity, and sustainability, is widely recognized as an ideal clean energy carrier to replace traditional fossil fuels [8–14]. Electrochemical overall water splitting (OWS) provides a highly attractive technical route for the large-scale production of green H_2, thanks to its distinctive merits of zero carbon emissions throughout the process, high-purity products, and direct compatibility with renewable energy sources [15–17]. This technology enables the simultaneous realization of the hydrogen evolution reaction (HER) at the cathode and the oxygen evolution reaction (OER) at the anode within a single electrolysis system, directly yielding high-purity hydrogen [18–20]. It not only effectively overcomes the drawbacks of conventional hydrogen production processes such as high carbon emissions, severe pollution, and reliance on fossil feedstocks, but also can be fully driven by intermittent clean energy sources including solar, wind, and hydro energy, truly realizing a closed-loop production model of green hydrogen generated from green electricity [21–23].

At present, the core challenges in OWS center on the relatively slow dynamics of both the cathodic HER and the anodic OER [24]. Particularly, the OER process, which involves multi-electron transfer, has a higher energy barrier and exhibits even slower kinetics, significantly limiting improvements in overall electrolysis efficiency [25–27].

✉ Xiaoqiang Du
duxq16@nuc.edu.cn

[1] School of Chemistry and Chemical Engineering, North University of China, Xueyuan road 3, Taiyuan 030051, People's Republic of China

[2] School of Environment and Safety Engineering, North University of China, Xueyuan road 3, Taiyuan 030051, People's Republic of China

Published online: 13 August 2026

Therefore, exploring environmentally friendly and durable OER electrodes is of great importance to realize high-performance water electrolysis [28]. Although precious -metal oxides for instance IrO_2 and RuO_2 show outstanding oxygen evolution activity, their prohibitive cost and limited natural resources greatly restrict their practical application on an industrial scale [29–31]. Another critical constraint for overall water splitting is the imbalance between the supply and demand of freshwater resources. The continuous consumption of freshwater has long exceeded the natural renewal capacity of renewable water resources [32]. In contrast, seawater accounts for approximately 97% of the Earth's total water resources, featuring an extremely large reserve and high accessibility [33, 34]. However, seawater has a complex composition, especially abundant chloride anions, which not only causes electrode corrosion but also triggers intense competitive side reactions with OER via the chlorine evolution reaction (ClER) [35–37]. Under alkaline conditions, a large amount of chloride ions in seawater can be readily oxidized to Cl_2 or ClO^- at a theoretical potential of 1.72 V, which is considerably higher than the 1.23 V theoretical potential for the OER [38–41]. Consequently, rationally designing high-performance and low-cost anode catalysts for both freshwater and seawater electrolysis, enhancing the intrinsic selectivity toward the OER in seawater, and kinetically suppressing the ClER have become urgent and critical tasks to be addressed at the current stage.

In recent years, fourth-period transition metal compounds, which are abundant in reserves, possess diverse oxidation states and are low in cost, have emerged as highly promising candidates to replace conventional high-performance water-splitting catalysts. Among them, transition metal sulfides [42], carbides, nitrides and phosphides [43] have been widely applied in the field for electrolysis of water [44–47]. Existing studies have confirmed that transition metal sulfides (TMS) possess a narrow band gap between the conduction band and valence band, thus exhibiting excellent electrical conductivity and typical semiconductor-like properties, which can effectively ensure rapid charge transport and interfacial electron transfer during electrocatalysis [48, 49]. Meanwhile, transition metal sulfides show certain advantages in synthesis and application compared with phosphides, carbides and nitrides. Phosphides tend to release toxic gases during high-temperature preparation, posing potential safety hazards. Carbide and nitride materials typically necessitate severe preparation conditions with ultrahigh temperature and pressure. In contrast, transition metal sulfides not only feature higher safety and milder, more controllable synthesis conditions, but also possess a large specific surface area and sufficient reaction centers for hydrogen adsorption, attracting extensive attention in the field of electrocatalysis. Among these, Ni_3S_2 is a highly representative material among metal sulfides. Its unique Ni-S coordination environment and three-dimensional network structure endow it with distinct metallic characteristics and superior electrical conductivity. These structural features can significantly accelerate charge transfer and interfacial reaction kinetics during electrocatalysis [50–52]. However, pure Ni_3S_2 often suffers from insufficient active sites, easy surface oxidation and passivation, and unsatisfactory long-term stability in electrocatalytic processes [53–56]. He et al. prepared an Al-Ni_3S_2/NF bifunctional catalyst via a hydrothermal method, which exhibited extraordinary electrocatalytic activity toward HER and OER simultaneously, achieving small overpotentials of 86 mV and 223 mV at 10 mA cm^{-2} [57]. Yan et al. successfully synthesized Mo, Fe-doped Ni_3S_2 nanoarrays, which delivered remarkable high-current OER activity under alkaline media, requiring overpotentials of merely 234 mV and 253 mV at 100 mA cm^{-2} and 200 mA cm^{-2}, respectively. In addition, the material also performed excellently in the HER, with an overpotential of only 59 mV at 10 mA cm^{-2}. Furthermore, to attain overall water splitting, the catalyst only consumes 1.45 V and 1.47 V in 1.0 M KOH solution and alkaline seawater separately [58]. Although important progress has been made in existing studies, the industrialization level in this domain still requires further advancement. On the basis of current research, this study takes Ni_3S_2 as the core target material, expecting to offer solid technical support for the robust transformation and utilization of sustainable energy resources through the development of novel catalytic materials.

In this work, we successfully fabricated Cr-VO_2/Ni_3S_2 multi-interfacial heterostructured composites via a one-step hydrothermal strategy. The abundant heterogeneous interfaces and porous structure endow the catalyst with rich active sites, which facilitate efficient internal charge transport, full contact between reactants, and effective utilization of active centers. The material can efficiently drive freshwater and seawater electrolysis in alkaline media, exhibiting outstanding OER catalytic performance. The catalyst achieves 10 mA cm^{-2} at an overpotential of 163 mV in 1 M KOH and exhibits stable performance during 15 h durability evaluation. In 1 M KOH-containing seawater, only 165 mV overpotential is required to drive the OER at 10 mA cm^{-2}. Density functional theory (DFT) analysis further verify that the Cr-VO_2 component in Cr-VO_2/Ni_3S_2 can effectively optimize the interfacial charge transfer dynamics and greatly enhance the water adsorption affinity of the catalyst. This study creates a novel strategy to boost the intrinsic catalytic activity of TMS in freshwater and seawater electrolysis.

Experimental section

Preprocessing operation of Ni foam (NF)

A 3 cm × 6 cm piece of nickel foam underwent ultrasonic cleaning in 3 mol/L HCl solution and ethanol for 15 min sequentially to strip surface oxide films and contaminants. The clean foamed Ni was then washed alternately with deionized H_2O and anhydrous C_2H_5OH, dried at 60 °C, and naturally cooled for further application.

Preparation of materials

Cr-VO_2/Ni_3S_2: First, A total of 1 mmol NH_4VO_3 and 0.3 mmol $Cr(NO_3)_3 \cdot 9H_2O$ were fully dissolved in 80 mL deionized H_2O, followed by dropwise addition of 2 mL ammonium hydroxide. Next, 0.56 g CH_3CSNH_2 was added into the mixed system, with continuous stirring carried out for 30 min to ensure uniform mixing. A pre-treated nickel foam was transferred into a 100 mL stainless steel autoclave with a Teflon inner liner, accompanied by the aforementioned precursor liquid., and kept at 160 °C for 5 h for a constant-temperature hydrothermal reaction. Finally, Cr-VO_2/Ni_3S_2 was successfully loaded onto the nickel foam.

The preparation of Co-VO_2/Ni_3S_2 was identical except that $Cr(NO_3)_3 \cdot 9H_2O$ was replaced by $Co(NO_3)_2 \cdot 6H_2O$. The synthetic procedures for VO_2/Ni_3S_2 and Ni_3S_2 were exactly the same, and the corresponding components were simply excluded from the precursor solution preparation process, respectively.

Results and discussion

Preparation and characterizations of the electrodes

Figure 1a shows a schematic illustration of the formation process of Cr-VO_2/Ni_3S_2. Cr-VO_2/Ni_3S_2 was grown in situ on Ni foam using a one-step hydrothermal method. In this reaction, $Cr(NO_3)_3 \cdot 9H_2O$ and NH_4VO_3 served as the sources of chromium and vanadium, respectively, while CH_3CSNH_2 acted as the sulfur source, slowly releasing sulfide ions under hydrothermal conditions to form the sulfide phase. $NH_3 \cdot H_2O$ was used to adjust the solution pH and promote the uniform dissolution of metal precursors, facilitating the formation of well-morphological and uniformly structured Cr-VO_2/Ni_3S_2 nanospheres on the NF substrate.

The phase constituents and crystal composition of the electrodes were characterized by X-ray diffraction (XRD) measurement. As presented in the XRD patterns (Fig. 1b), three major diffraction signals at 44.49°, 51.84° and 76.38° can be indexed to the (111), (200) and (220) facets of the nickel foam base material (PDF#87–0712). In addition, Sharp diffraction signals appear at 21.7°, 31.1°, 37.7°, 49.7° and 55.1°, which can be indexed to the (101), (110), (003), (113) and (122) crystal planes of Ni_3S_2 (PDF#44-1418). The characteristic diffraction peak appearing at 49.6° corresponds to the (421) plane of VO_2 (PDF#42–0876). These results verify the successful preparation of Cr-VO_2/Ni_3S_2, Co-VO_2/Ni_3S_2, VO_2/Ni_3S_2, and Ni_3S_2.

Scanning electron microscopy (SEM) was implemented to study and investigate the micromorphology of the as-prepared electrodes. The SEM images of the samples at scales of 1 μm, 500 nm, and 200 nm are depicted in the Fig. 1(c-h). As displayed in Fig. 1(c-e), VO_2/Ni_3S_2 exhibits a three-dimensional nanosphere microstructure assembled from nanoparticles with tight stacking between particles. In contrast, as displayed in Fig. 1(f-h), the introduction of Cr significantly regulates the morphology of material. The surface of Cr-doped nanoparticles is obviously roughened with abundant wrinkles. This Cr-induced rough morphology not only effectively enlarges the electrochemically active surface area but also exposes more edge active sites. Fig. S1(a–c) shows that the Ni_3S_2 material presents a continuous and uniform film-like morphology with a dense surface and rich textures, without obvious cracks or severe agglomeration. Fig. S1(d–f) reveals that the Co-VO_2/Ni_3S_2 material possesses a nanosphere morphology.

The fine microstructural features of the electrodes were comprehensively explored via transmission electron microscopy (TEM) and high-resolution transmission electron microscopy (HRTEM). Lattice fringes of the catalyst can be readily noticed in the HRTEM images. A distinct heterostructure interface between VO_2 and Ni_3S_2 is visible in Fig. 2a. A lattice spacing of 0.20 nm in Fig. 2b is consistent with the (202) plane of Ni_3S_2, whereas the 0.29 nm lattice spacing in Fig. 2c corresponds to the (220) crystal plane of VO_2. The green dashed line in Fig. 2a clearly marks the closely contacted heterojunction interface between VO_2 and Ni_3S_2, which reveals robust electronic interaction formation at the heterointerfaces of the two phases. Such interfacial coupling can effectively modulate the interfacial electronic structure and accelerate charge transfer across the interface. These lattice fringe spacings also offer solid evidence for the successful formation of VO_2 and Ni_3S_2 crystalline phases. The elemental composition and proportion in Cr-VO_2/Ni_3S_2 were determined by EDS spectrum analysis (Fig. S2). As displayed in Fig. 2(d-h), the elemental mapping proves that Cr, V, O, Ni and S are homogeneously distributed on the surface of the Cr-VO_2/Ni_3S_2 composite.

The surface elemental components, chemical valence and coordination surroundings of Cr-VO_2/Ni_3S_2 and VO_2/Ni_3S_2 were comprehensively analyzed via X-ray photoelectron spectroscopy (XPS) measurement, so as to gain in-depth

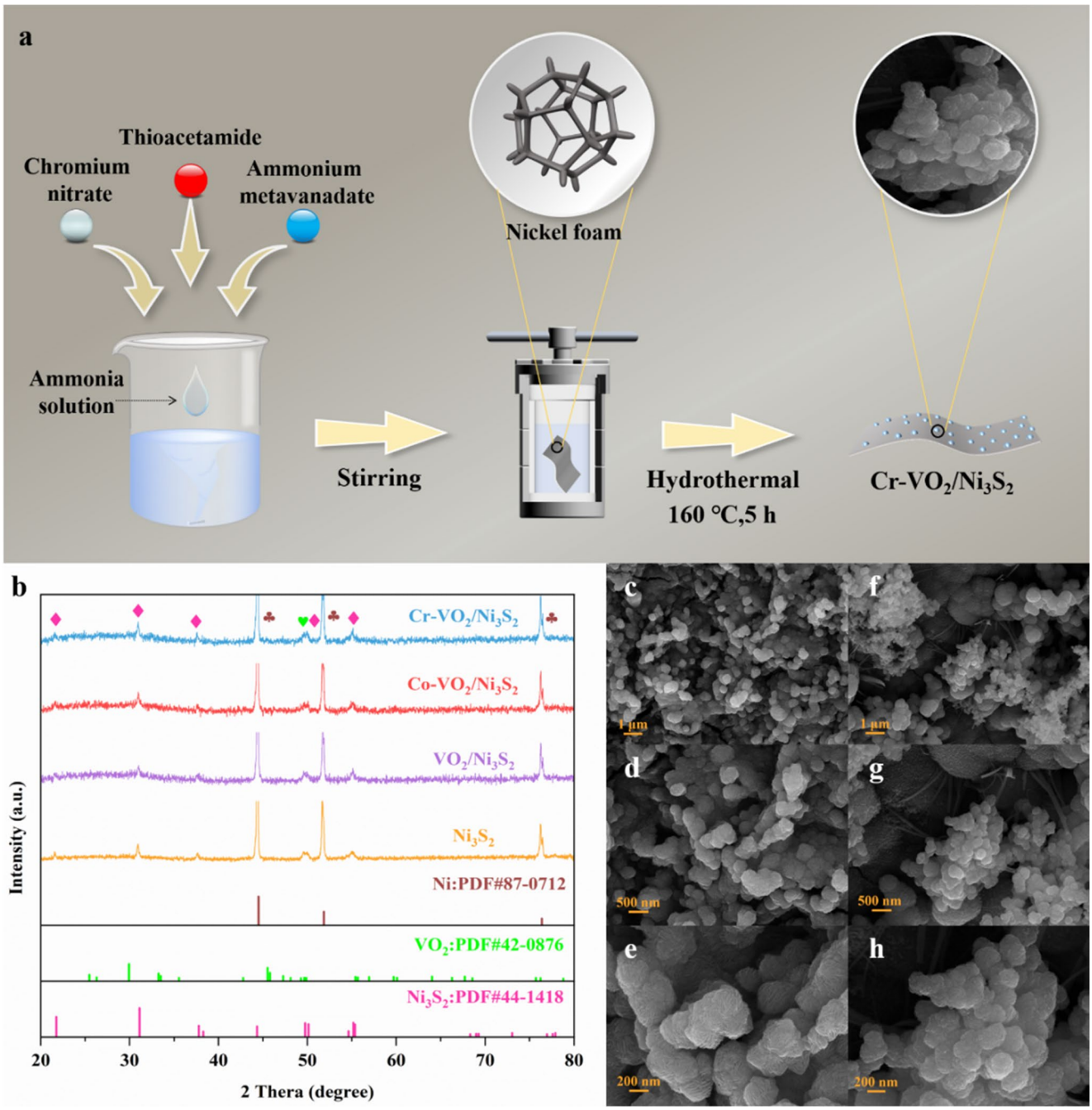

Fig. 1 (**a**) Schematic diagram of the synthesis of Cr-VO_2/Ni_3S_2 electrocatalytic material. (**b**) XRD patterns of Cr-VO_2/Ni_3S_2, Co-VO_2/Ni_3S_2, VO_2/Ni_3S_2 and Ni_3S_2. (**c-e**) SEM images of VO_2/Ni_3S_2. (**f-h**) SEM images of Cr-VO_2/Ni_3S_2

insights into the surface electronic structure of the materials. The full XPS survey spectra of Cr-VO_2/Ni_3S_2 and VO_2/Ni_3S_2 shown in Fig. 3a clearly confirm the coexistence of Cr, V, O, Ni, and S elements in Cr-VO_2/Ni_3S_2. The elemental distribution is highly consistent with the EDS results, further verifying the successful fabrication and elemental composition of the material. The Cr 2p spectrum of Cr-VO_2/Ni_3S_2 (Fig. 3b) displays two typical peaks at 577.55 eV and 587.04 eV, which are assigned to the Cr^{3+} $2p_{3/2}$ and $2p_{1/2}$ orbits [59]. From the V 2p spectrum of Cr-VO_2/Ni_3S_2 (Fig. 3c), 515.57 eV and 522.64 eV are characteristic of V^{3+} $2p_{3/2}$ and $2p_{1/2}$; 516.51 eV and 523.98 eV match the 2p orbitals of V^{4+}; and 517.37 eV together with 524.72 eV correspond to the $2p_{3/2}$ and $2p_{1/2}$ components of V^{5+} [60]. Two distinct peaks can be observed in the O 1s spectrum (Fig. 3d) at 530.14 eV and 531.03 eV, which is originating from metal-oxygen bonds and non-lattice oxygen respectively. Meanwhile, the peak centered at 532.49 eV is

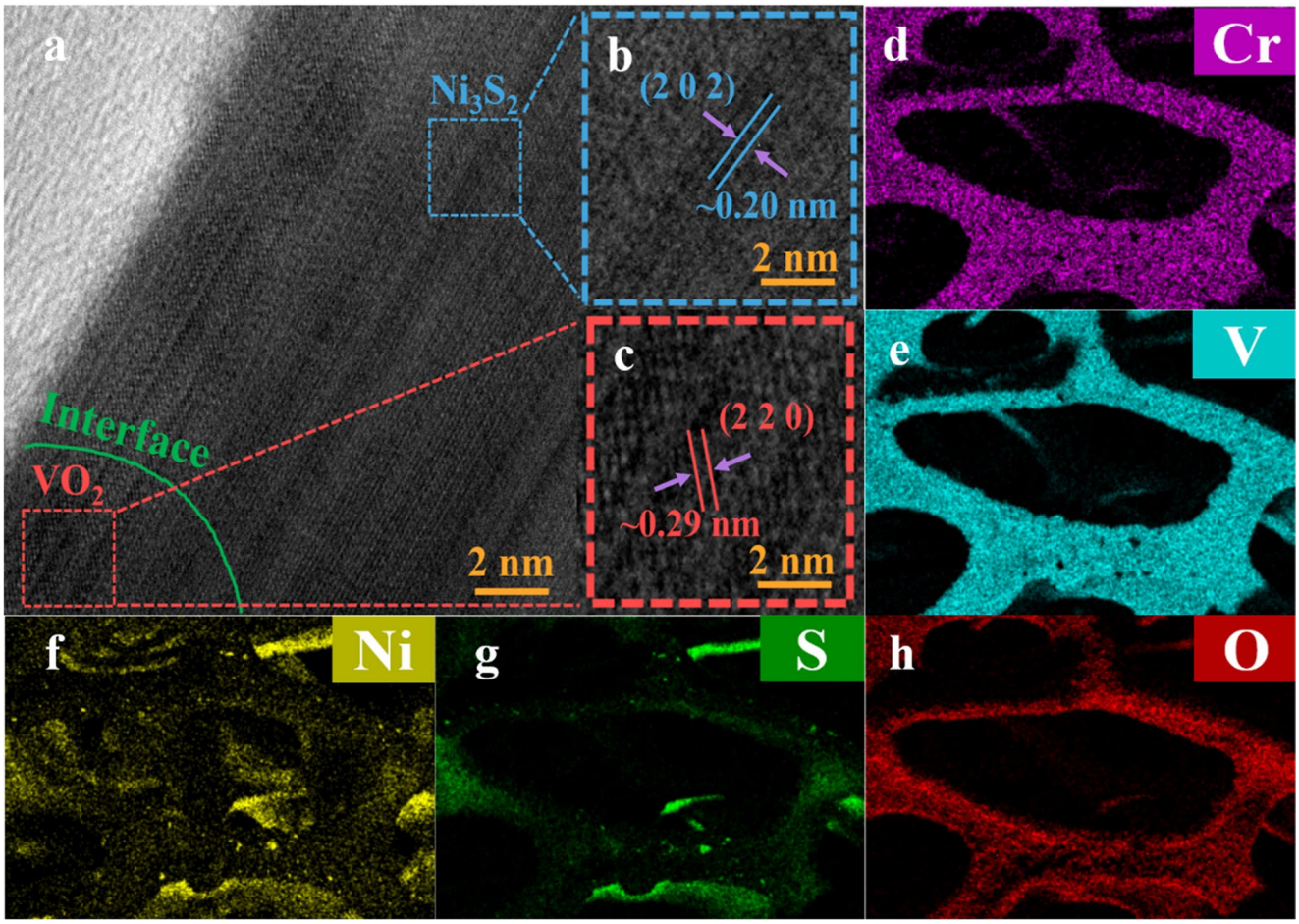

Fig. 2 (**a**-**c**) HR-TEM of Cr-VO_2/Ni_3S_2. (**d**-**h**) EDS mapping of (**d**) Cr, (**e**) V, (f) Ni, (**g**) S and (**h**) O in Cr-VO_2/Ni_3S_2

indexed to surface chemisorbed oxygen. The enrichment of non-lattice oxygen and chemisorbed oxygen can not only effectively expose more catalytic active sites but also accelerate charge transfer and intermediate adsorption during the reaction, thus promoting the electrocatalytic performance [61–63]. For the high-resolution Ni 2p spectrum (Fig. 3e), the Ni $2p_{3/2}$ and $2p_{1/2}$ signals can be fitted into three major components together with their satellite counterparts. The signals located at 852.88 eV and 870.43 eV belong to elemental metallic Ni(0). In addition, the doublet peaks at 855.96 eV and 873.55 eV are indexed to Ni^{2+}, and another pair at 857.30 eV and 875.07 eV is characteristic of Ni^{3+}. The binding energies of 861.92 eV and 880.21 eV correspond to the satellite peaks for Ni $2p_{3/2}$ and Ni $2p_{1/2}$ orbitals [64–66]. Notably, compared with VO_2/Ni_3S_2, the binding energy of the Ni 2p peaks in Cr-VO_2/Ni_3S_2 shifts toward higher values, accompanied by an increased ratio of Ni^{2+} to Ni^{3+}, indicating electron transfer from Ni to Cr and V sites. This establishes strong interfacial electronic interactions and optimizes the electronic environment of the active sites. Figure 3f displays the S 2p spectrum, the binding energy of 167.39 eV can be attributed to S-O species, while the two typical peaks at 161.99 eV and 163.46 eV belong to Ni-S bonds [67, 68]. After Cr doping, the intensity of the Ni-S peaks in Cr-VO_2/Ni_3S_2 is enhanced relative to VO_2/Ni_3S_2, whereas the S-O peak is weakened, suggesting that Cr doping stabilizes the sulfide structure of Ni_3S_2, reduces surface oxidation, and improves the structural stability of the material. XPS investigations demonstrate that the Cr-VO_2/Ni_3S_2 heterostructure effectively regulates the electronic structure and significantly promotes the intrinsic electrocatalytic performance of the catalyst.

OER activity in alkaline freshwater

A conventional three-electrode setup was used to evaluate the oxygen evolution reaction (OER) electrocatalytic activity of the obtained electrodes in 1 M KOH electrolyte. Linear sweep voltammetry (LSV) was used to record polarization curves, intuitively reflecting the variation trend of current density against applied potential. As shown in Fig. 4a, Cr-VO_2/Ni_3S_2 required an overpotential of only 163 mV to deliver 10 mA cm^{-2} for OER, which was

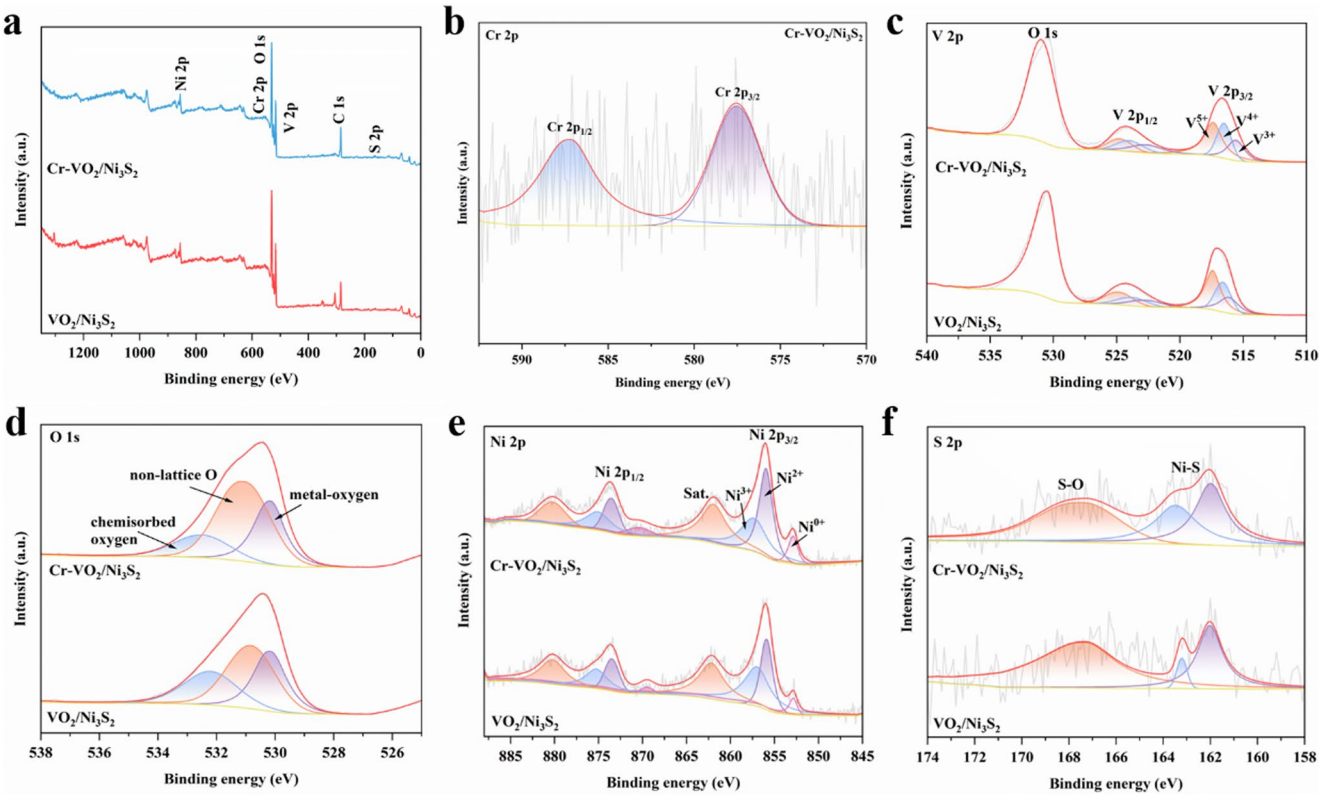

Fig. 3 XPS spectra of Cr-VO_2/Ni_3S_2 and VO_2/Ni_3S_2 (**a**) Survey spectra, (**b**) Cr 2p, (**c**) V 2p, (**d**) O 1s, (**e**) Ni 2p and (**f**) S 2p

considerably lower than 197 mV for Co-VO_2/Ni_3S_2, 203 mV for VO_2/Ni_3S_2, and 361 mV for Ni_3S_2. A comparison of overpotentials for different catalysts at 10, 50 and 100 mA cm^{-2} is presented in Fig. 4b. It is evident that the Cr-VO_2/Ni_3S_2 composite exhibits the lowest overpotential to reach the targeted current density relative to other counterparts. Furthermore, the kinetic characteristics of the electrocatalytic reaction were further analyzed by comparing the Tafel slopes of each sample. Tafel curve analysis (Fig. 4c) shows that the Tafel slope of Cr-VO_2/Ni_3S_2 was 75.65 mV dec^{-1}, the smallest among all catalysts, which is lower than 125.32 mV dec^{-1} for Co-VO_2/Ni_3S_2, 161.86 mV dec^{-1} for VO_2/Ni_3S_2, and 172.86 mV dec^{-1} for Ni_3S_2. Smaller Tafel slopes correspond to faster reaction kinetics for electron and proton transport, reflecting superior reaction dynamics. In addition, as presented in Fig. 4d and Table S1, the OER catalytic performance of Cr-VO_2/Ni_3S_2 in this work is comparable to recently reported high-performance OER electrocatalysts, fully demonstrating its promising application potential and competitiveness in electrocatalysis. Next, Cyclic voltammetry curves were recorded at multiple sweep rates of 20–100 mV s^{-1} (Fig. S3) for electrochemical active surface area (ECSA) evaluation. The C_{dl} value was acquired by fitting the capacitive current in the non-Faradaic potential window. As displayed in Fig. 4e, the Cr-VO_2/Ni_3S_2 sample exhibited the largest C_{dl} value of 9.39 mF cm^{-2}, which was not only larger than that of Co-VO_2/Ni_3S_2 (7.45 mF cm^{-2}) but also significantly superior to VO_2/Ni_3S_2 (3.40 mF cm^{-2}) and Ni_3S_2 (2.73 mF cm^{-2}). The higher C_{dl} value directly reflects that Cr-VO_2/Ni_3S_2 possesses a higher effective contact area and more abundant catalytic reaction centres, which constitutes the structural basis for its excellent electrocatalytic performance. From the electrochemical impedance spectroscopy (EIS) in Fig. 4f, Cr-VO_2/Ni_3S_2 exhibited the smallest semicircle radius, which was remarkably smaller than that of pure Ni_3S_2. This result fully proves that the synergistic effect of Cr introduction and the heterointerfaces can effectively decrease the interfacial charge-transfer resistance and accelerate electron transport and reaction kinetics. A high-performance catalyst should exhibit both superior catalytic activity and robust electrochemical durability. Therefore, the electrochemical durability in 1 M KOH solution was systematically evaluated. As clearly observed in Fig. 4g, the Cr-VO_2/Ni_3S_2 catalyst exhibits acceptable stability. After a long-term durability test of 15 h at a constant current density, the catalyst still maintained relatively stable electrochemical performance, with a reasonable current decay and no obvious sudden activity loss, fully reflecting its electrochemical durability. After the chronoamperometry test, LSV measurements were conducted on the catalyst. As shown in Fig. 4h, the catalytic activity decreased slightly compared with the initial sample before the test, further

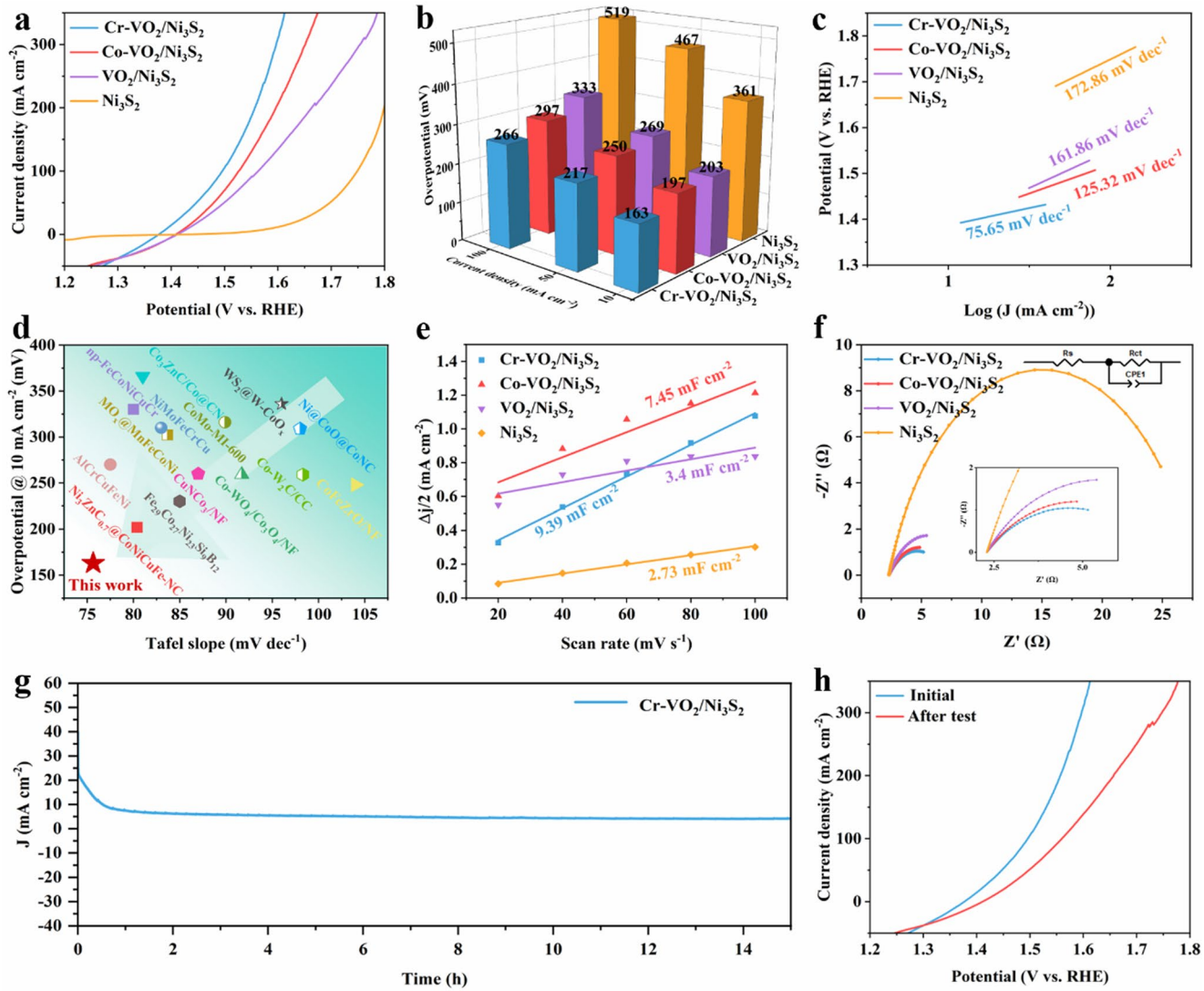

Fig. 4 The electrochemical performances in 1 M KOH solution. (**a**) Polarization curve of LSV; (**b**) Comparison of the overpotential at 10, 50 and 100 mA cm^{-2}; (**c**) Tafel slope; (**d**) Comparison of freshwater electrolysis performance between Cr-VO_2/Ni_3S_2 and previously reported materials. (**e**) Double-layer capacitances of the electrodes; (**f**) Nyquist curve; (**g**) Chronocurrent curve of Cr-VO_2/Ni_3S_2; (**h**) LSV comparison for initial and recovered electrode

confirming that Cr-VO_2/Ni_3S_2 can retain its catalytic activity relatively stable during the 15-hour long-term electrochemical reaction.

Furthermore, systematic structural and morphological characterizations were performed on the catalyst after the stability test. Fig. S4 displays the XRD patterns of the catalyst before and after long-term OER stability measurement. The initial sample exhibits characteristic diffraction peaks of Ni_3S_2, VO_2, and nickel foam support. After the alkaline OER durability test, all diffraction signals originating from the VO_2 phase completely vanish. This phenomenon can be attributed to the VO_2 active layer on the catalyst surface being subjected to continuous scouring by bubbles and corrosion from the strongly alkaline environment during long-term OER, resulting in partial dissolution, flaking, or detachment. In contrast, the diffraction peaks of Ni_3S_2 and Ni foam substrate can still be clearly observed, with no obvious shift or attenuation. Fig. S5 displays the comparison of SEM images of the electrode before and after the durability measurement. Compared with the pristine morphology before reaction, the microstructure of the catalyst was well preserved, and the nanoparticles were still uniformly distributed on the substrate surface. Only minor local cracks were observed, which may originate from stress variation during electrolysis without damaging the structural integrity. To further explore the surface chemical stability and valence state evolution mechanism of the Cr-VO_2/Ni_3S_2 heterostructured catalyst during long-term OER, XPS characterization was performed on the samples before and after the stability test, as presented in the Fig. S6. The full XPS

spectrum (Fig. S6a) presents that Ni, Cr, O, V and S were still present after long-term OER, but with reduced peak intensities, indicating slight element leaching or limited structural damage during the prolonged test. As presented in Fig. S6b, the peak intensity decreased slightly while the peak positions remained generally stable compared with the initial sample, revealing that the Cr species maintained good chemical stability after the reaction. In Fig. S6c, the characteristic peaks of V 2p almost completely disappeared after the stability test, with only the O 1s signal retained. This can be attributed to partial dissolution, exfoliation, or detachment of the VO_2 active layer rich in V on the catalyst surface, caused by bubble scouring and strong alkaline etching during long-term OER, leading to reduced surface V content and thus significantly attenuated V 2p signal in XPS. As illustrated in Fig. S6d, a reduction in the relative content of the metal-oxygen peak was detected in the O 1s spectrum, clearly demonstrating the surface oxidation of the electrode during the OER process. Fig. S6e presents the Ni 2p spectra before and after reaction. The characteristic peak of Ni^{0+} completely disappeared after the stability test, indicating that Ni^{0+} was fully oxidized to Ni^{2+} and Ni^{3+} during the oxidation process. In the S 2p spectrum (Fig. S6f), the intensity of characteristic peaks for Ni-S has decreased significantly, but their positions were almost unchanged, suggesting that to a certain extent, the internal Ni_3S_2 structure of the catalyst was preserved during long-term electrocatalysis. Meanwhile, the peak area assigned to S-O decreased slightly, which is a normal result of unavoidable element loss during prolonged electrocatalytic testing.

To reveal the modulation mechanism of Cr doping on the interfacial kinetics between the electrolyte and catalyst, EIS measurements were performed on Cr-VO_2/Ni_3S_2 and VO_2/Ni_3S_2 at various applied potentials. As observed from the Nyquist plots in Fig. 5a and b, the semicircle diameters of both catalysts gradually decrease with the increase of applied potential, demonstrating a pronounced reduction in charge transfer resistance and weakened kinetic resistance during the reaction. Figure 5c and d present the Bode plots of Cr-VO_2/Ni_3S_2 and VO_2/Ni_3S_2, respectively. EIS comparison shows the Nyquist arc of Cr-VO_2/Ni_3S_2 is obviously smaller than that of VO_2/Ni_3S_2. It proves that the incorporation of Cr can remarkably diminish charge transfer resistance, improve electron conduction at the solid-liquid interface, and further promote the kinetic process of OER interfacial charge transfer. As shown in Fig. 5e, the variations in phase angle peaks of Cr-VO_2/Ni_3S_2 and VO_2/Ni_3S_2 at different potentials were compared. Within the tested potential range, Cr-VO_2/Ni_3S_2 always displays a distinctly lower phase angle peak than VO_2/Ni_3S_2. Overall, Cr doping effectively optimizes the interfacial charge kinetics of VO_2/Ni_3S_2, creates abundant active sites and high-efficiency electron transport pathways on the electrode surface, and lowers the charge transfer resistance.

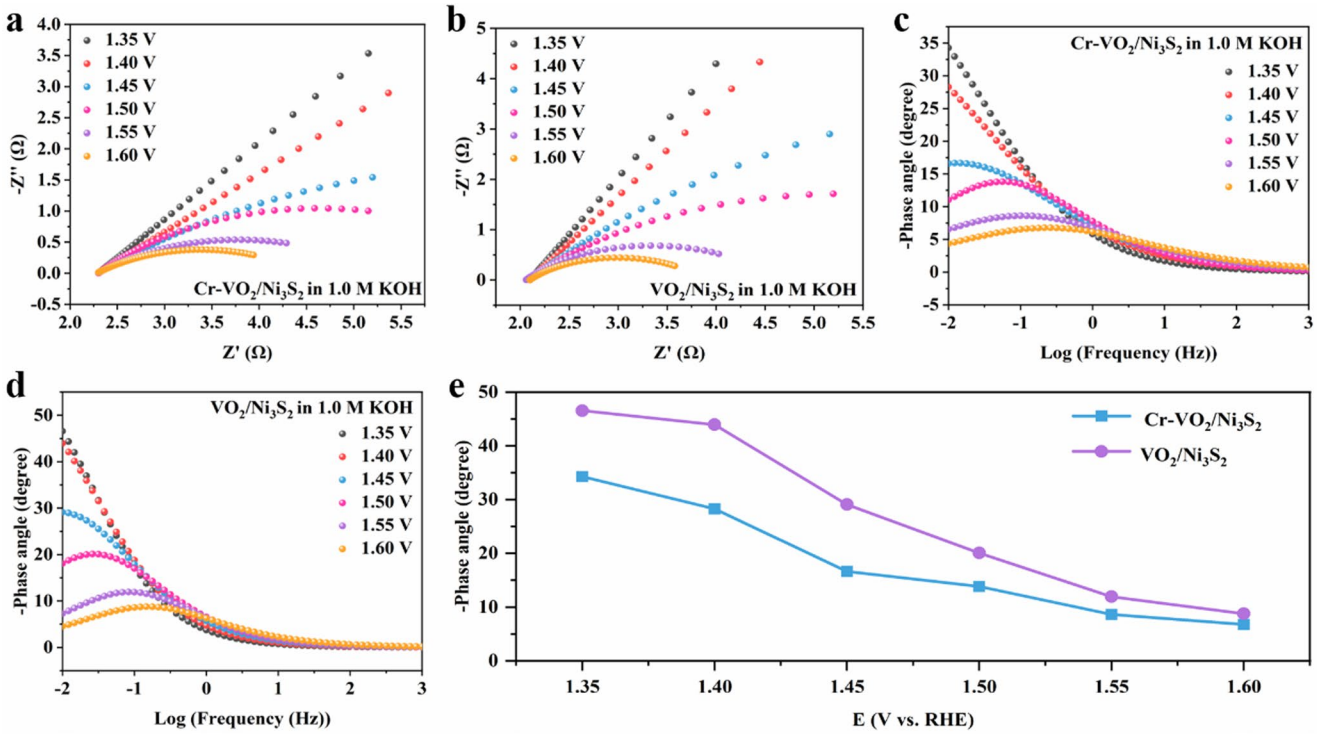

Fig. 5 (**a**) EIS spectra of Cr-VO_2/Ni_3S_2 and (**b**) VO_2/Ni_3S_2 at multiple voltages in 1.0 M KOH. (**c**) Bode plots of Cr-VO_2/Ni_3S_2 and (**d**) VO_2/Ni_3S_2. (**e**) Peak phase angles of Cr-VO_2/Ni_3S_2 and VO_2/Ni_3S_2

OER performance in seawater

Given the outstanding OER activity and stability of Cr-VO_2/Ni_3S_2 in 1 M KOH freshwater electrolyte, its OER performance was further evaluated in seawater-based electrolyte. The core bottleneck of seawater electrolysis lies in the fierce competition between the OER and chlorine evolution reaction (ClER) under acidic conditions, while chlorine oxidation to form hypochlorite by-products readily occurs in alkaline media. These parasitic reaction pathways severely degrade the overall energy efficiency of seawater oxidation. Herein, the electrochemistry performance of the as-fabricated electrodes was studied in alkaline natural seawater solution (1 M KOH + natural seawater). As shown in Fig. 6a, Cr-VO_2/Ni_3S_2 required an overpotential of 165 mV to reach 10 mA cm^{-2}. This value is slightly larger than that in freshwater systems, but much lower than 190 mV for Co-VO_2/Ni_3S_2, 209 mV for VO_2/Ni_3S_2, and 263 mV for pure Ni_3S_2. Figure 6b demonstrates that Cr-VO_2/Ni_3S_2 delivers the smallest overpotential at 10, 50, and 100 mA cm^{-2}. Furthermore, a comparison with recently reported advanced OER electrocatalysts confirms the superior overpotential performance of Cr-VO_2/Ni_3S_2 at 10 mA cm^{-2}, as summarized in Fig. 6e and Table S2. The Tafel plots in Fig. 6c reveal that Cr-VO_2/Ni_3S_2 possesses a low Tafel slope of 85.34 mV dec^{-1}, which is much smaller than those of Co-VO_2/Ni_3S_2 (131.42 mV dec^{-1}), VO_2/Ni_3S_2 (170.28 mV dec^{-1}), and Ni_3S_2 (267.84 mV dec^{-1}), demonstrating the favorable OER kinetics of Cr-VO_2/Ni_3S_2. The electrochemical C_{dl} was estimated from CV curves (Fig. S7). As presented in Fig. 6d, Cr-VO_2/Ni_3S_2 achieves a high C_{dl} of 14.93 mF cm^{-2}, outperforming Co-VO_2/Ni_3S_2 (12.09 mF

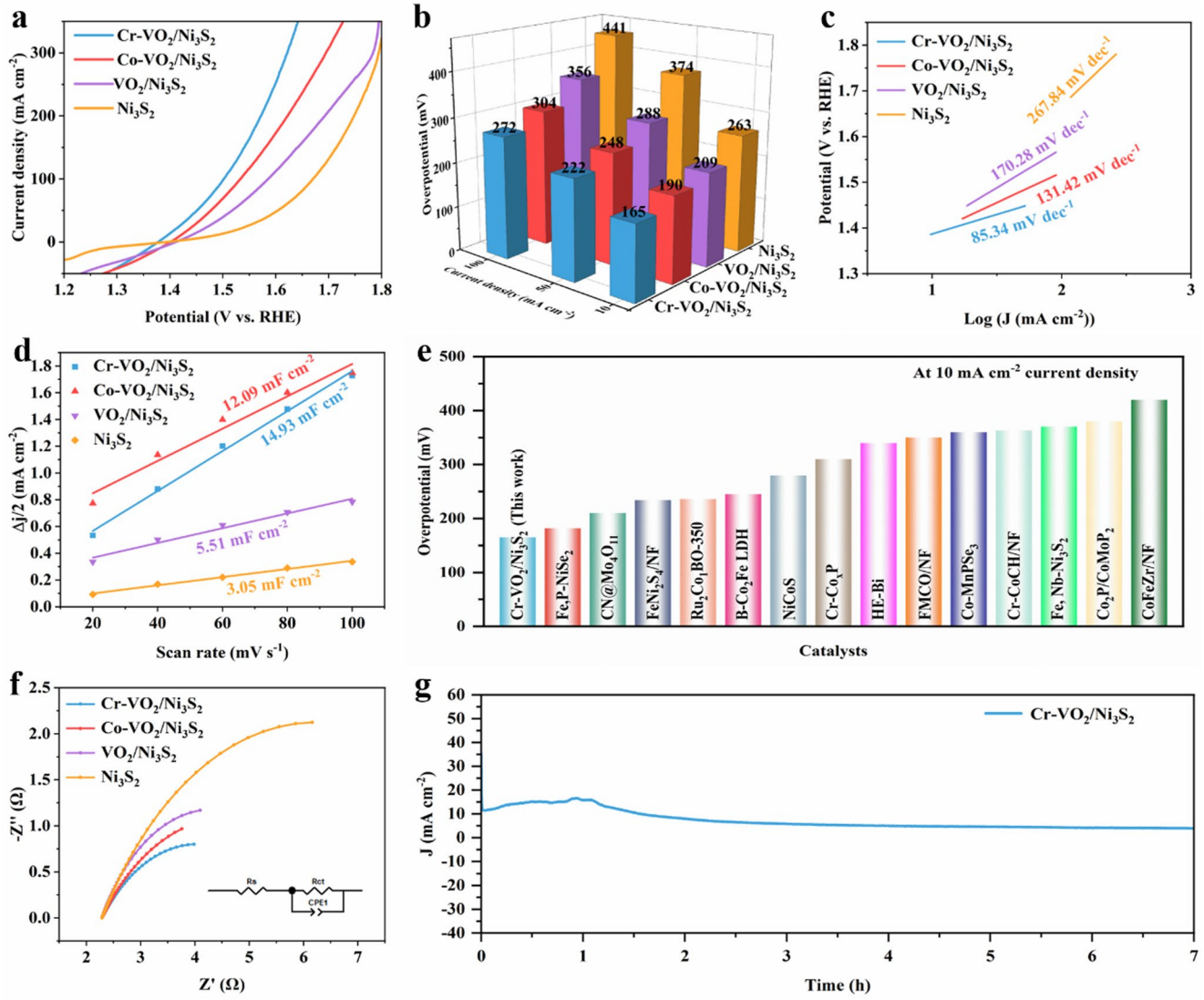

Fig. 6 The electrochemical performances in 1 M KOH + seawater solution. (**a**) Polarization curve of LSV; (**b**) Comparison of the overpotential at 10, 50 and 100 mA cm^{-2}; (**c**) Tafel slope; (**d**) Double-layer capacitances of the electrodes; (**e**) Comparison of seawater electrolysis performance between Cr-VO_2/Ni_3S_2 and previously reported materials. (**f**) Nyquist curve; (**g**) Chronocurrent curve of Cr-VO_2/Ni_3S_2

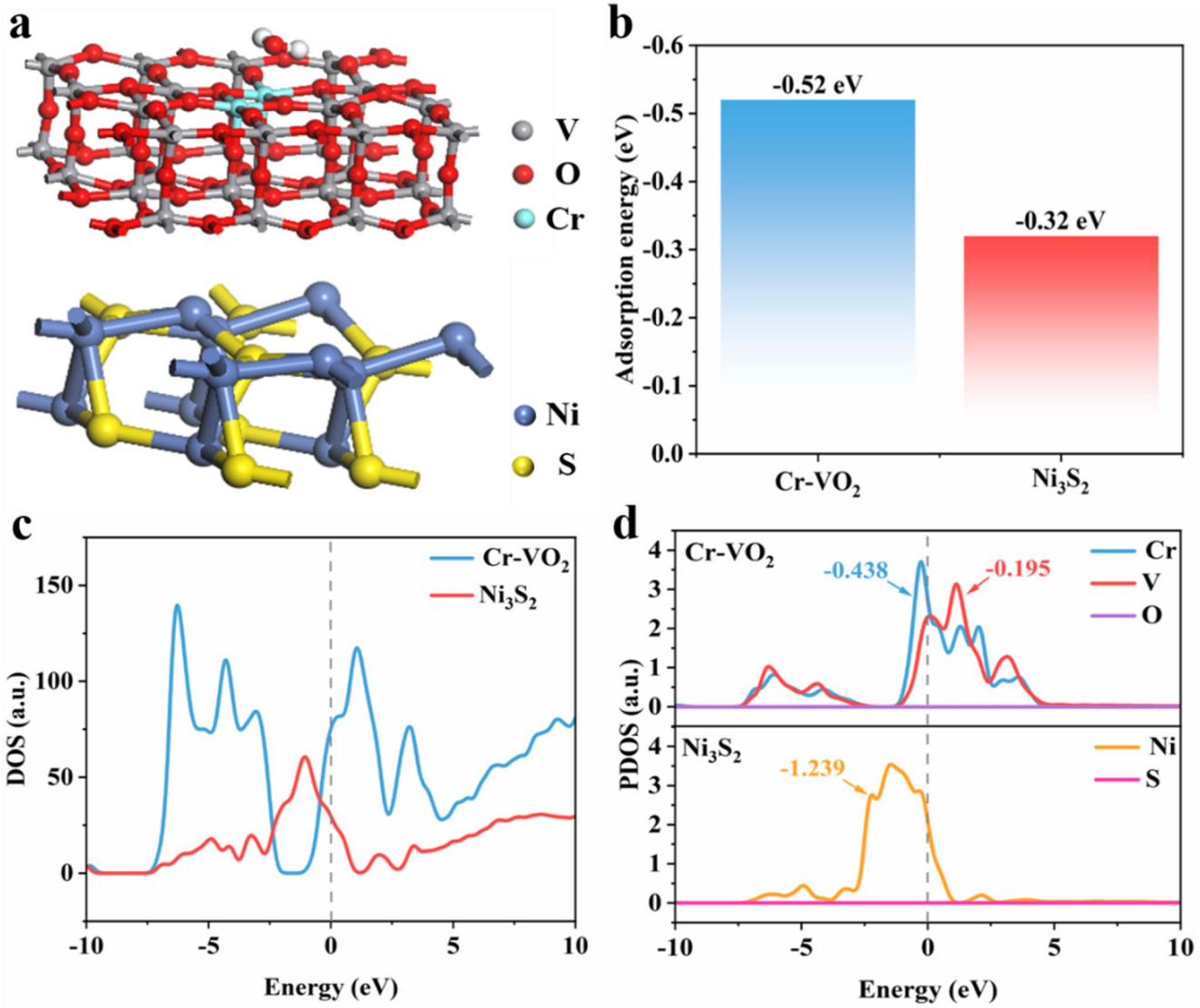

Fig. 7 (**a**) Geometric models of H_2O adsorption on Cr-VO_2 and Ni_3S_2, (**b**) H_2O adsorption energy on Cr-VO_2 and Ni_3S_2 samples, (**c**) DOS of Cr-VO_2 and Ni_3S_2, (**d**) PDOS of on Cr-VO_2 and Ni_3S_2

cm^{-2}), VO_2/Ni_3S_2 (5.51 mF cm^{-2}) and Ni_3S_2 (3.05 mF cm^{-2}). This result verifies the enlarged electrochemical active surface area of Cr-VO_2/Ni_3S_2, which benefits from the nanosphere structure assembled from interconnected nanoparticles and affords abundant accessible active sites. EIS was adopted to further reveal the kinetic behavior and charge transfer resistance of the as-prepared catalysts. EIS results (Fig. 6f) show that Cr-VO_2/Ni_3S_2 exhibits the smallest semicircle radius and charge transfer resistance, indicative of rapid interfacial electron transport. The long-term durability of Cr-VO_2/Ni_3S_2 was also measured in 1 M KOH alkaline seawater. As presented in Fig. 6g, no obvious activity degradation is observated after 7 h of continuous operation at a constant current density, proving its acceptable durability in harsh seawater electrolysis conditions. In summary, the as-prepared Cr-VO_2/Ni_3S_2 catalyst also presents remarkable OER performance in 1 M KOH alkaline seawater electrolyte.

DFT calculations

Density functional theory (DFT) analysis were performed to clarify the underlying relationship between the electronic structure of Cr-VO_2/Ni_3S_2 and the enhanced electrocatalytic OER performance [69]. We have also built a model of heterogeneous interfaces, but after optimizing it many times, it always reports errors. Figure 7a displays the optimized atomic models of Cr-doped VO_2 and Ni_3S_2 surfaces, clearly presenting the spatial distribution of V, O, Cr, Ni, and S atoms at the heterogeneous interface. Figure 7b presents

the adsorption energy values for Cr-VO_2 and Ni_3S_2, which are −0.52 eV and −0.32 eV in turn. This result reveal that Cr-VO_2 possesses an intensified adsorption capability, enabling easier adsorption of water molecules on its surface. This active component effectively optimizes the water activation ability of the Cr-VO_2/Ni_3S_2 catalyst, thereby synergistically improving the overall electrocatalytic reaction kinetics and catalytic activity. Density of states (DOS) calculations were further employed to analyze the electronic properties of the two components. It can be seen from Fig. 7c that Cr-VO_2 exhibits a broader and more continuous density of states distribution near the Fermi level. Its unique electronic structure endows the composite with excellent intrinsic conductivity, which accelerates charge transfer during the OER process and remarkably boosts the reaction kinetic rate. In order to clarify the internal origin of the boosted catalytic performance of Cr-VO_2/Ni_3S_2 at a deeper level, partial density of states (PDOS) calculations were adopted to compare the electronic structural characteristics of diverse active centers. The d-band center (ε_d) serves as a crucial descriptor correlated with the adsorption behavior of intermediates. Its position relative to the Fermi level fundamentally influences the bonding strength of the catalyst with oxygenated reaction intermediates, including OH*, O*, and OOH*. A d-band center closer to the Fermi level corresponds to more prominent interfacial adsorption interaction [70, 71]. As illustrated in Fig. 7d, the d-band centers of Cr, V, and Ni are −0.438 eV, -0.195 eV, and −1.239 eV, respectively. The above results confirm that the Cr sites in Cr-VO_2 and the Ni sites in Ni_3S_2 collectively constitute the main active centers of the Cr-VO_2/Ni_3S_2 catalyst. In addition, Fig. S8 and S9 present the PDOS of each element in Cr-VO_2 and Ni_3S_2, respectively. The analysis indicates that the electronic states of Cr, V, and Ni are mainly dominated by d orbitals, while the bonding processes of O and S elements primarily rely on p orbitals. In summary, the superior water adsorption and activation ability as well as intrinsic conductivity of Cr-doped VO_2 endow Cr-VO_2/Ni_3S_2 with outstanding OER electrocatalytic performance.

Conclusion

In summary, Cr-VO_2/Ni_3S_2 heterostructured catalysts were directly fabricated on NF through the use of a one-step hydrothermal process. In 1 M KOH electrolyte, Cr-VO_2/Ni_3S_2 only requires an overpotential of 163 mV to deliver 10 mA cm^{-2}. In 1.0 M KOH seawater electrolyte, the overpotential of Cr-VO_2/Ni_3S_2 at 10 mA cm^{-2} is as low as 165 mV for OER. Electrochemical analysis reveals that the superior overpotential and reaction kinetics of the catalyst originate intrinsically from its unique hierarchical structure and efficient charge transport capability. DFT calculations demonstrate that the Cr-VO_2 component in Cr-VO_2/Ni_3S_2 can effectively accelerate charge transfer and exhibits remarkably enhanced adsorption capability toward water molecules. This work not only opens up a novel strategy for the construction of high-efficiency electrodes for electrolysis of water, but also facilitates the long-term development of renewable energy storage and conversion technologies.

Supplementary Information The online version contains supplementary material available at https://doi.org/10.1007/s11581-026-07454-7.

Acknowledgements This work is supported by National Natural Science Foundation of China (Grant No. 52305622), and the China Postdoctoral Science Foundation (Grant No. 2024M763033, 2025T180150). The authors extend their gratitude to Ms. Shaoyuan Guo (from Scientific Compass www.shiyanjia.com) for providing invaluable assistance with the SEM analysis.

Author contributions "Haonan Wang and Huipeng Zhao wrote the main manuscript text and Xiaoshuang Zhang and Xiaoqiang Du prepared figures 1-7. All authors reviewed the manuscript."

Data availability No datasets were generated or analysed during the current study.

Declarations

Competing interests The authors declare no competing interests.

References

1. Xue Q, Sun HY, Li YN, Zhong MJ, Li FM, Tian XL, Chen P, Yin SB, Chen Y (2021) Au@Ir core-shell nanowires towards oxygen reduction reaction. Chem Eng J 421:129760
2. Fan JL, Fu CY, Liang RK, Lv HY, Fang CS, Guo YH, Hao WJ (2022) Mild construction of midas touch metal-organic framework-based catalytic electrodes for highly efficient overall seawater splitting. Small 18:2203588
3. Gu CJ, Zhou GY, Yang J, Pang H, Zhang MY, Zhao Q, Gu XF, Tian S, Zhang JB, Xu L, Tang YW (2022) NiS/MoS_2 Mott-Schottky heterojunction-induced local charge redistribution for high-efficiency urea-assisted energy-saving hydrogen production. Chem Eng J 443:136321
4. Jin X, Wang XF, Liu YL, Kim MJ, Cao M, Xie HH, Liu ST, Wang XB, Huang W, Nanjundan AK, Yuliarto B, Li XY, Yamauchi Y (2022) Nitrogen and sulfur co-doped hierarchically porous carbon nanotubes for fast potassium ion storage. Small 18:2203545
5. Sun LT, Liang XL, Liu HM, Cao HJ, Liu XH, Jin Y, Li XY, Chen S, Wu XD (2023) Activation of Co-O bond in (110) facet exposed Co_3O_4 by Cu doping for the boost of propane catalytic oxidation. J Hazard Mater 452:131319
6. Guo H, Shi Q, Xu Y, Yue G, Liang Z, Yue C, Ye S, Liu Q, Wei Q, Yang D, Yang W (2026) Direct activation of layered double hydroxides for efficient and durable water splitting at high current densities. Appl Catal B: Environ Energy 380:125774
7. Liu WH, Li W, Liang Z, Feng YF, Ye SB, Yue CC, Ming R, Lu XY, Yang WY, Shi Q (2025) Se-vacancy induced structural reconstruction of iron nickel selenium nanosheets for efficient and durable electrocatalytic alkaline water and seawater oxidation. J Mater Chem A 13:10934–10944

8. Fu GD, Kang XM, Zhang Y, Yang XQ, Wang L, Fu XZ, Zhang JJ, Luo JL, Liu JW (2022) Coordination effect-promoted durable $Ni(OH)_2$ for energy-saving hydrogen evolution from water/methanol co-electrocatalysis. Nano-Micro Lett 14:200
9. Yu WL, Chen Z, Fu YL, Xiao WP, Dong B, Chai YM, Wu ZX, Wang L (2023) Superb All-pH hydrogen evolution performances powered by ultralow Pt-decorated hierarchical Ni-Mo porous microcolumns. Adv Funct Mater 33:2210855
10. Wu ZX, Yang PF, Li QC, Xiao WP, Li ZJ, Xu GR, Liu FS, Jia BH, Ma TY, Feng SH, Wang L (2023) Microwave synthesis of Pt clusters on black TiO_2 with abundant oxygen vacancies for efficient acidic electrocatalytic hydrogen evolution. Angew Chem Int Ed 62:e202300406
11. Wu ZX, Gao YX, Wang ZX, Xiao WP, Wang XP, Li B, Li ZJ, Liu XB, Ma TY, Wang L (2023) Surface-enriched ultrafine Pt nanoparticles coupled with defective CoP as efficient trifunctional electrocatalyst for overall water splitting and flexible Zn-air battery. Chin J Catal 46:36–47
12. Shen P, Zhou BW, Chen Z, Xiao WP, Fu YL, Wan J, Wu ZX, Wang L (2023) Ruthenium-doped 3D Cu_2O nanochains as efficient electrocatalyst towards hydrogen evolution and hydrazine oxidation. Appl Catal B: Environ Energy 325:122305
13. Ye SB, Xu Y, Bai XY, Liang Z, Liu Q, Wei QL, Yang DJ, Yang WY, Gao FM, Shi Q (2025) Efficient bifunctional water splitting catalysts enabled by crystalline-amorphous Ni_xS_y@NiFe LDH heterojunctions. J Mater Chem A 13:16143–16154
14. Yue CC, Liang Z, Xu Y, Liu Q, Wei QL, Yang DJ, Du JJ, Yang WY, Shi Q (2025) Synergistic heterojunctions of $CoSe_2$ and NiFe layed double hydroxide: bridging in situ phase evolution and charge redistribution as bifunctional catalysts for water splitting. J Colloid Interface Sci 699:138252
15. Zhang H, Zhou YT, Xu M, Chen A, Ni ZT, Akdim O, Wagberg T, Huang XY, Hu GZ (2023) Interface engineering on amorphous/crystalline hydroxides/sulfides heterostructure nanoarrays for enhanced solar water splitting. ACS Nano 17:636–647
16. Wang BY, Schlegel N, Aalling-Frederiksen O, Berner E, Zhang DM, Pittkowski RK, Jensen KMO, Arenz M (2024) $(Ni_{1-x}Fe_x)$ OOH binary nanoparticles in as-prepared and purified KOH electrolyte solutions for water splitting. ACS Appl Nano Mater 7:12345–12355
17. Nguyen TTA, Tran KD, Tran DT, Sidra S, Kim D, Kim NH, Lee JH (2025) Tunable catalytic performance on iridium clusters-interspersed CoxSy-CoO nanosheet-built hollows for enhanced water splitting. Small 21:2412435
18. Cui BH, Shi Y, Li G, Chen YN, Chen W, Deng YD, Hu WB (2022) Challenges and opportunities for seawater electrolysis: A mini-review on advanced materials in chlorine-involved electrochemistry. Acta Phys -Chim Sin 38:2106010
19. Liang J, Cai ZW, Li ZX, Yao YC, Luo YS, Sun SJ, Zheng DD, Liu Q, Sun XP, Tang B (2024) Efficient bubble/precipitate traffic enables stable seawater reduction electrocatalysis at industrial-level current densities. Nat Commun 15:2950
20. Liang J, Li J, Dong H, Li Z, He X, Wang Y, Yao Y, Ren Y, Sun S, Luo Y, Zheng D, Li J, Liu Q, Luo F, Wu T, Chen G, Sun X, Tang B (2024) Aqueous alternating electrolysis prolongs electrode lifespans under harsh operation conditions. Nat commun 15:6208
21. Haase FT, Bergmann A, Jones TE, Timoshenko J, Herzog A, Jeon HS, Rettenmaier C (2022) Roldan Cuenya, Size effects and active state formation of cobalt oxide nanoparticles during the oxygen evolution reaction. Nat Energy 7:765–773
22. Karacan C, Lohmann-Richters FP, Keeley GP, Scheepers F, Shviro M, Müller M, Carmo M, Stolten D (2022) Challenges and important considerations when benchmarking single-cell alkaline electrolyzers. Int J Hydrogen Energy 47:4294–4303
23. Wu JD, Wang DP, Wan S, Liu HLL, Wang C, Wang X (2022) An efficient cobalt phosphide electrocatalyst derived from cobalt phosphonate complex for all-pH hydrogen evolution reaction and overall water splitting in alkaline solution. Small 18:2202883
24. Dong KX, Tran DT, Li X, Prabhakaran S, Kim D, Kim NH, Lee JH (2024) Three-phase interface engineering via P-doped $CoMo_2S_4$-integrated Co_4S_3/Co_2P enables high-efficiency overall water splitting. Appl Catal B: Environ Energy 344:123649
25. Liu MH, Chen XX, Li SY, Ni CD, Chen YW, Su H (2024) Dynamic-cycling zinc sites promote ruthenium oxide for sub-ampere electrochemical water oxidation. Nano Lett 24:16055–16063
26. Han LL, Guo LM, Dong CQ, Zhang C, Gao H, Niu JZ, Peng ZQ, Zhang ZH (2019) Ternary mesoporous cobalt-iron-nickel oxide efficiently catalyzing oxygen/hydrogen evolution reactions and overall water splitting. Nano Res 12:2281–2287
27. Sun HM, Yan ZH, Liu FM, Xu WC, Cheng FY, Chen J (2020) Self-supported transition-metal-based electrocatalysts for hydrogen and oxygen evolution. Adv Mater 32:1806326
28. Li WX, Liu Y, Azam A, Liu YC, Yang J, Wang DY, Sorrell CC, Zhao C, Li S (2024) Unlocking efficiency: Minimizing energy loss in electrocatalysts for water splitting. Adv Mater 36:2404658
29. Tran KD, Nguyen TH, Tran DT, Dinh VA, Kim NH, Lee JH (2024) Realizing the tailored catalytic performances on atomic Pt-promoted transition metal moieties implanted layered double hydroxides for water electrolysis. ACS Nano 18:16222–16235
30. Xiong J, Yan CY, Liu W, Guo XX, Ma J, Yi WT, Han MF (2021) Insights into the principles, design methodology and applications of electrocatalysts towards hydrogen evolution reaction. Energy Rep 7:8577–8596
31. Balaji R, Nguyen TT, Ngo QP, Kim NH, Lee JH (2024) Unveiling the synergistic mechanism of atomic Rh on couple phase $CoSe_2$/$CoSeO_3$ for enhanced alkaline water electrolysis devices. Adv Funct Mater 34:2410672
32. Tong WM, Forster M, Dionigi F, Dresp S, Erami RS, Strasser P, Cowan AJ, Farràs P (2020) Electrolysis of low-grade and saline surface water. Nat Energy 5:367–377
33. Li YY, Zhou H, Cai SH, Prabhakaran D, Niu WT, Large A, Held G, Taylor RA, Wu XP, Tsang SCE (2024) Electrolyte-assisted polarization leading to enhanced charge separation and solar-to-hydrogen conversion efficiency of seawater splitting. Nat Catal 7:77–88
34. Chen WX, Wei W, Li F, Wang YJ, Liu M, Dong S, Cui JH, Zhang YY, Wang R, Ostrikov K, Zang SQ (2024) Tunable built-in electric field in ru nanoclusters-based electrocatalyst boosts water splitting and simulated seawater electrolysis. Adv Funct Mater 34:2310690
35. Zhang W, Chen WJ, Xiao Q, Yu L, Huang CQ, Lu GX, Morawski AW, Yu Y (2020) Nitrogen-coordinated metallic cobalt disulfide self-encapsulated in graphitic carbon for electrochemical water oxidation. Appl Catal B: Environ Energy 268:118449
36. Fan RL, Liu CH, Li ZH, Huang HT, Feng JY, Li ZS, Zou ZG (2024) Ultrastable electrocatalytic seawater splitting at ampere-level current density. Nat Sust 7:158–167
37. Haq TU, Haik Y (2022) Strategies of anode design for seawater electrolysis: Recent development and future perspective. Small Sci 2:2200030
38. Fang B, Chu X, Han XX, He JN, Geng BK, Jia LX, Wang X, Song SY, Zhang HJ (2022) Incorporation of CeO_2 with Ni-Co mixed metal phosphide boosts electrochemical seawater oxidation performance. Chem Commun 58:13803–13806
39. Zhang FH, Yu L, Wu LB, Luo D, Ren ZF (2021) Rational design of oxygen evolution reaction catalysts for seawater electrolysis. Trends Chem 3:485–498
40. Bollu M, Tran DT, Prabhakaran S, Kim D, Kim NH, Lee JH (2024) Continuously interconnected network enabled by Pt single atoms-promoted CoNiP-CoNi heterostructures for efficient water electrolysis. Nano Energy 123:109413

41. Wang HY, Sun ML, Ren JT, Yuan ZY (2023) Circumventing challenges: Design of anodic electrocatalysts for hybrid water electrolysis systems. Adv Energy Mater 13:2203568
42. Du X, Ding Y, Zhang X (2023) MOF-derived Zn–Co–Ni sulfides with hollow nanosword arrays for high-efficiency overall water and urea electrolysis. Green Energy Environ 8:798–811
43. Ren YC, Song JY, Sun SJ, Li ZX, Yang CX, Cai ZW, Zhang M, Yue M, Wang HF, Zheng DD, Lv YQ, Sun XP, Tang B (2025) A hierarchical NiPOx@NiFe LDH nanoarray for durable seawater oxidation. J Colloid Interface Sci 687:708–714
44. Wu LB, Yu L, Zhang FH, McElhenny B, Luo D, Karim A, Chen S, Ren ZF (2021) Heterogeneous bimetallic phosphide Ni_2P-Fe_2P as an efficient bifunctional catalyst for water/seawater splitting. Adv Funct Mater 31:2006484
45. Yu L, Zhu Q, Song SW, McElhenny B, Wang DZ, Wu CZ, Qin ZJ, Bao JM, Yu Y, Chen S, Ren ZF (2019) Non-noble metal-nitride based electrocatalysts for high-performance alkaline seawater electrolysis. Nat Commun 10:5106
46. Ali A, Long F, Shen PK (2022) Innovative strategies for overall water splitting using nanostructured transition metal electrocatalysts, Electrochem. Energy Rev 5:1
47. Niu S, Jiang WJ, Wei ZX, Tang T, Ma JM, Hu JS, Wan LJ (2019) Se-doping activates FeOOH for cost-effective and efficient electrochemical water oxidation. J Am Chem Soc 141:7005–7013
48. Khalil A, Liu Q, Muhammad Z, Habib M, Khan R, He Q, Fang Q, Masood HT, Rehman ZU, Xiang T, Wu CQ, Song L (2017) Synthesis of Ni9S8/MoS2 heterocatalyst for enhanced hydrogen evolution reaction. Langmuir 33:5148–5153
49. Zheng Y, Jiao Y, Jaroniec M, Qiao SZ (2015) Advancing the electrochemistry of the hydrogen-evolution reaction through combining experiment and theory. Angew Chem Int Ed 54:52–65
50. Li DR, Wan WJ, Wang ZW, Wu HY, Wu SX, Jiang T, Cai GX, Jiang CZ, Ren F (2022) Self-derivation and surface reconstruction of Fe-Doped Ni_3S_2 electrode realizing high-efficient and stable overall water and urea electrolysis. Adv Energy Mater 12:2201913
51. Feng LL, Yu GT, Wu YY, Li GD, Li H, Sun YH, Asefa T, Chen W, Zou XX (2015) High-index faceted Ni_3S_2 nanosheet arrays as highly active and ultrastable electrocatalysts for water splitting. J Am Chem Soc 137:14023–14026
52. Dong J, Zhang FQ, Yang Y, Zhang YB, He HL, Huang XF, Fan XJ, Zhang XM (2019) (003)-Facet-exposed Ni_3S_2 nanoporous thin films on nickel foil for efficient water splitting. Appl Catal B 243:693–702
53. Ha QN, Gultom NS, Silitonga MZ, Gemeda TN, Kuo DH (2023) Novel core-shell structure of Ni_3S_2@LiMoNiOx(OH)y nanorod arrays toward efficient high-current-density hydrogen evolution reaction. Chem Eng J 467:143253
54. Zhang K, Duan YX, Graham N, Yu WZ (2023) Unveiling the synergy of polymorph heterointerface and sulfur vacancy in NiS/Ni_3S_2 electrocatalyst to promote alkaline hydrogen evolution reaction. Appl Catal B: Environ Energy 323:122144
55. Gultom NS, Li CH, Kuo DH, Abdullah H (2022) Single-step synthesis of Fe-Doped Ni_3S_2/FeS_2 nanocomposites for highly efficient oxygen evolution reaction. ACS Appl Mater Interfaces 14:39917–39926
56. Ha QN, Gultom NS, Yeh CH, Kuo DH (2023) One-pot synthesized Li, V co-doped Ni_3S_2 nanorod arrays as a bifunctional electrocatalyst for industrialization-facile hydrogen production via alkaline exchange membrane water electrolysis. Chem Eng J 472:144931
57. He WJ, Wang FQ, Jia DB, Li Y, Liang LM, Zhang J, Hao QY, Liu CC, Liu H, Zhao JL (2020) Al-doped nickel sulfide nanosheet arrays as highly efficient bifunctional electrocatalysts for overall water splitting. Nanoscale 12:24244–24250
58. Sang Y, Xue JW, Hu JJ, Chen LJ (2025) High-current density alkaline water/seawater splitting by Mo and Fe co-doped Ni_3S_2:Invariant active sites with accelerated water dissociation kinetics. Appl Catal B: Environ Energy 361:124698
59. Song YY, Sun MZ, Zhang SC, Zhang XY, Yi P, Liu JZ, Huang BL, Huang MH, Zhang LX (2023) Alleviating the work function of vein-like Co_XP by Cr doping for enhanced seawater electrolysis. Adv Funct Mater 33:2214081
60. Fan K, Ji YF, Zou HY, Zhang JF, Zhu BC, Chen H, Daniel Q, Luo Y, Yu JG, Sun LC (2017) Hollow iron-vanadium composite spheres: A highly efficient iron-based water oxidation electrocatalyst without the need for nickel or cobalt. Angew Chem Int Ed 56:3289–3293
61. Yu TQ, Xu QL, Chen JL, Qian GF, Zhuo XY, Yang HF, Yin SB (2022) Boosting urea-assisted water splitting by constructing sphere-flower-like $NiSe_2$-$NiMoO_4$ heterostructure. Chem Eng J 449:137791
62. Guo PF, Liu GR, Yin J, Hu HX, Li EZ, Meng YT, Gao HJ, Wang WP, Li ZC (2024) Synthesis of MoO_3/N, P co-doped carbon for electrochemical water splitting. Fuel 355:129476
63. Zhang JY, Zhang SS, Zhang XF, Ma Z, Wang Z, Zhao B (2023) Construction of Ni_4Mo/MoO_2 heterostructure on oxygen vacancy enriched $NiMoO_4$ nanorods as an efficient bifunctional electrocatalyst for overall water splitting. J Colloid Interface Sci 650:1490–1499
64. Zhou JQ, Li PF, Xia XY, Zhao Y, Hu ZH, Xie YL, Yang L, Liu YS, Du Y, Zhou QC, Yu L, Yu Y (2024) Precisely tailoring the d-band center of nickel sulfide for boosting overall water splitting. Appl Catal B: Environ Energy 359:124461
65. Wang H, Du XQ, Zhang XS (2025) Transition metal-based selenide materials derived from ZIF-67 as efficient urea and seawater splitting electrocatalyst. Renewable Energy 244:122663
66. Kim M, Min K, Ko D, Seong H, Shim SE, Baeck SH (2023) Regulating the electronic structure of Ni_2P by one-step Co, N dual-doping for boosting electrocatalytic performance toward oxygen evolution reaction and urea oxidation reaction. J Colloid Interface Sci 650:1851–1861
67. Liu Q, Xie LS, Liu Z, Du G, Asiri AM, Sun XP (2017) A Zn-doped Ni_3S_2 nanosheet array as a high-performance electrochemical water oxidation catalyst in alkaline solution. Chem Commun 53:12446–12449
68. Huang SC, Meng YY, Cao YF, Yao F, He ZJ, Wang XX, Pan H, Wu MM (2020) Amorphous $NiWO_4$ nanoparticles boosting the alkaline hydrogen evolution performance of Ni_3S_2 electrocatalysts. Appl Catal B 274:119120
69. Sun J, Guo NK, Shao ZY, Huang KK, Li YW, He F, Wang Q (2018) A facile strategy to construct amorphous spinel-based electrocatalysts with massive oxygen vacancies using ionic liquid dopant. Adv Energy Mater 8:1800980
70. Ge WY, Lin LP, Wang SQ, Wang YC, Ma XW, An Q, Zhao L (2023) Electrocatalytic urea oxidation: advances in mechanistic insights, nanocatalyst design, and applications. J Mater Chem A 11:15100–15121
71. Jiang JB, Sun R, Huang X, Xu WX, Zhou SB, Wei Y, Han S, Li YL (2023) In-situ derived Mo-doped NiCoP and MXene to form Mott-Schottky heterojunction with tunable surface electron density to promote overall water splitting. Compos Part B 263:110834